FAULT DETECTION AND DIAGNOSIS FOR THERMAL MANAGEMENT SYSTEM IN ELECTRIFIED AIRCRAFT PROPULSION

Z. Barot*, R. Cepeda-Gomez*

* German Aerospace Center, Institute of Electrified Aero Engines, Department of Aeronautical Requirements and Control of Propulsion System, Lieberoser Straße 13A, Cottbus, Germany

Abstract

The thermal management system (TMS) of electrified aircraft propulsion (EAP) is critical to safety and efficiency, especially for hydrogen fuel-cell and battery configurations. While architecture optimisation has been widely studied, fault detection and diagnosis (FDD) of TMS components remains underexplored. Here, a model-based FDD framework that leverages analytical redundancy via a bank of unknown-input observers (UIOs) is proposed. Each UIO is designed on a linearised TMS model of a Polymer Electrolyte Membrane Fuel Cell to reject known disturbances and non–target actuator faults; residuals are formed as innovations and shaped by a left-nullspace projection to enforce selectivity. Detection uses a causal moving-average envelope and adaptive, robust thresholds based on median absolute deviation with persistence, improving detectability during take-off while curbing false alarms. For a realistic scenario, measurements are simulated with Gaussian sensor noise. Simulation-based single-fault injections show consistently high detection rates, short delays relative to system dynamics, negligible false alarms under influence of disturbance, and no cross-detections across observers, evidencing reliable isolation. A sensitivity limit is observed for a coolant-leak type fault, where detection rate reduces for fault magnitude below 50% of the coolant flow.

Keywords

Fault Detection and Diagnosis ; Thermal Management System ; Battery ; Hydrogen Fuel Cells ; Electrified Aircraft

1. INTRODUCTION

Hydrogen fuel cells, particularly proton exchange membrane fuel cells (PEMFC), are widely regarded as a promising energy conversion technology for future electric aircraft propulsion (EAP) [1]. The electrochemical process is conceptually simple: At the anode, hydrogen fuel is oxidized, separating into protons and electrons; the protons then travel through the proton exchange membrane to the cathode and recombine with oxygen to form water, releasing heat in the process. The electrons are forced through the external circuit to generate electric current. In practice, however, PEMFC systems are mechanically and thermally delicate due to the combined demands of high power density, rapid dynamic response, durability, and cost-effectiveness. A PEMFC produces almost as much waste heat as its electric power output, thus limiting its energy efficiency to about 50% [2]. Therefore, effective thermal management is recognised as one of the most critical technical challenges. Thermal Management Systems (TMS) scale with stack power; air-cooled stacks suffice only at low power ($\approx\leq$ 5 kW), whereas high-power systems, typical of EAP, require liquid or phase-change cooling loops to meet the heat-rejection demands [3]. For PEMFCs, stack temperature is crucial for performance and durability. Effective TMS control must therefore detect faults before they propagate and cause thermal runaways or accelerated degradation. The criticality of the TMS in PEMFC-powered aircraft extends beyond efficiency, as faults in TMS components, such as pumps, fans, heat exchangers, or coolant loops, can quickly lead to thermal instability, loss of efficiency, or even catastrophic failure. Since thermal faults can propagate rapidly, early stage detection is essential to prevent escalation and allow fault-tolerant control to maintain safe operation. Although fault detection and diagnosis (FDD) is well established in many aerospace subsystems, studies targeting TMS — particularly in the context of electrified aircraft — remain scarce.

Existing FDD approaches can be broadly categorized into signal-based, data-driven, and model-based methods. Signal-based techniques (e.g., spectral, wavelet, or Hilbert analysis) extract characteristic features from sensor signals, while data-driven methods employ machine learning or deep learning models to classify faults from large datasets. These approaches are effective when rich data are available but often lack robustness and physical interpretability. In contrast, model-based schemes exploit system dynamics to generate residuals, enabling reliable detection even under varying operating conditions, which makes them well suited for safety-critical applications such as PEMFC thermal management [4]. Model-based FDD uses analytical redundancy to compare measured and predicted behavior, generating residuals that enable early detection and isolation of faults. Canonical techniques include parameter estimation, parity relations, and observer-based schemes, which improve over simple limit checks especially for incipient faults and during transients [5]. Hashemi et al. [6] developed a fast model-based fault diagnosis method for lithium-ion batteries in electric and hybrid-electric aircraft. Utilizing an extended Kalman filter and multiple-model adaptive estimation, the approach efficiently detected overcharge, overdischarge, and sensor faults. Milfont et al. [7] reviewed fault diagnosis techniques for electric machines in aeronautical propulsion, focusing on permanent magnet synchronous machines and various methods such as model-based, signal-based, and machine learning approaches. They identified challenges in incipient fault detection, noise, and data limitations while also examining mechanical faults in bearings, gearboxes, and blades. Henry et al. [8] proposed a model-based fault detection scheme for early and robust fault diagnosis

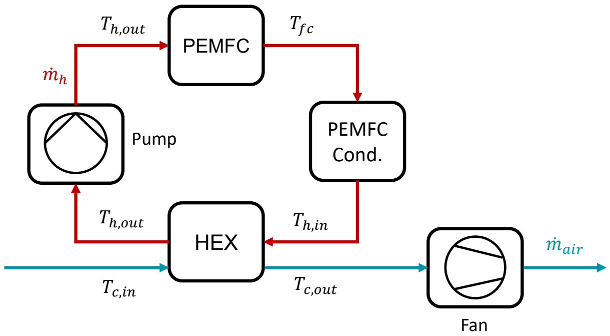

FIG 1. Baseline TMS architecture around PEMFC

in aircraft control surface servo-loops. Their method, based on the H_∞/H_2 design technique and μ_g analysis, effectively diagnosed faults such as aileron jamming and disconnections, as demonstrated using a high-fidelity Airbus simulator. Yan et al. [9] have demonstrated model-based FDD and fault-tolerant thermal control experimentally. In particular, Dulmage–Mendelsohn decomposition-guided residual generation have been used to detect sensor faults in the thermal loop, with closed-loop controllers maintaining stack temperature even under failures. Park et al. [10] described severity-based fault categorisation, which standardizes residuals, applies moving averages, and trains neural networks per severity tier. With this, they are able to trade sensitivity versus robustness across critical, significant, and minor faults, including multi-fault cases. Despite this progress, dedicated FDD for the TMS, especially in electrified aircraft settings with high heat flux, tight temperature windows, and strong propulsion-cooling coupling remains comparatively under-explored. The present work targets this gap with an observer-bank design, residual structuring, and robust threshold tailored to PEMFC TMS operation.

Components related to the TMS can be broadly categorized into two groups: those requiring TMS (e.g., batteries, fuel cells, motors) and those enabling it (e.g., fans, pumps, cooling loops, heat exchangers) [11]. This paper presents a simulation-validated FDD framework for a PEMFC TMS focused on actuator-side faults relevant to aircraft integration. The main contributions include:

- a bank of Unknown Input Observers (UIO) for each fault which enforces disturbance rejection and cross-fault decoupling in the observer error dynamics,
- a residual projection that builds structured residuals and are provably blind to non-target signatures yet sensitive to the intended fault, and
- robust thresholds based on median absolute-deviation with persistence to avoid false alarms during transients.

The approach is evaluated via simulated faulty measurement data under varying thermal loads. It also reports detection times and isolation performance for the observer bank. Sections 2.1-2.3 detail the state space modelling of TMS components and their interconnections. The definition of UIO bank, residuals, and fault detection logic is described in sections 2.4-2.5. The performance of the presented FDD approach is discussed in section 3. The conclusions and future outlook are discussed in section 4.

2. METHODOLOGY

Figure 1 shows the baseline architecture [12] of the TMS around a PEMFC stack, for which the FDD algorithm is developed. For this work, the take-off phase is considered as the operating point, stack temperature is considered equal to the coolant temperature exiting from the stack, and the measurements are assumed to be noisy and but no sensor faults are present. It is also assumed, that only one actuator fault happens at a time. Synthetic measurement data based on a simulated non-linear model is used for validation of the algorithm.

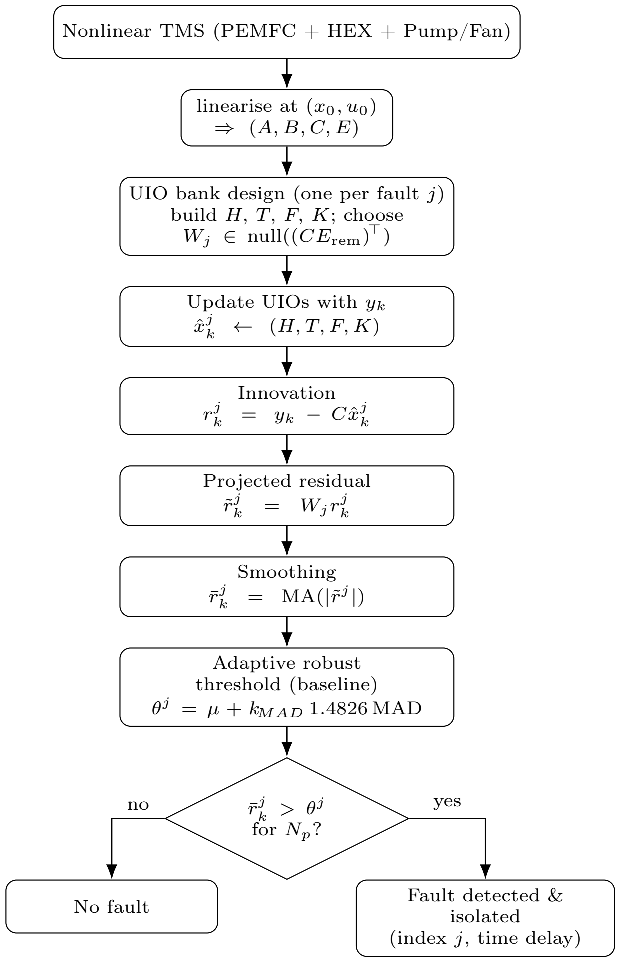

FIG 2. Overview of fault detection via UIO bank and threshold design

The flowchart presented in figure 2 depicts the whole process of the proposed UIO based actuator fault detection. First, the TMS is modeled based on baseline architecture in subsection 2.1. Then, the model is converted into a state space model and linearised, in subsection 2.3, around the operating point for the observer design. In subsection 2.4, UIO bank is designed for different faults and residual conditioning and threshold generation from the non-faulty data is explained in subsection 2.5.

2.1. TMS modelling

As shown in figure 1, the hot loop (coolant loop) extracts heat from the stack (Q_{pemfc}) and rejects it partially by preheating the PEMFC inlet hydrogen fuel and air ($Q_{\mathrm{conditioning}}$). The remaining heat is rejected through a cross-flow heat exchanger (HEX) to the cold loop (air loop). The actuators are the coolant pump and axial fan, which drive the coolant mass flow $\dot{m}_h$ and air mass flow $\dot{m}_{\mathrm{air}}$, respectively. The measured temperatures are the stack temperature, T_{fc}, the temperature of the coolant exiting from the HEX, $T_{\mathrm{h,out}}$, and the temperature of the

TAB 1. Key constants used in UIO-based fault detection (non-sensitive subset).

Symbol	Description	Units	Nominal value
$t_{\rm s}$	Sampling time	s	2×10^{-3}
$T_{\rm fc}$	Stack temperature	K	353.15
$T_{\rm c,in}$	air inlet temperature	K	303.15
$C_{\rm th,fc} = m_{\rm fc} c_{p,\rm fc}$	Stack thermal capacitance	J/K	6.93×10^5
$c_{p,\rm air}$	Air specific heat	J/(kg K)	1005
$c_{p,\rm coolant}$	Coolant specific heat	J/(kg K)	3550
$\rho_{\rm coolant}$	Coolant density	kg/m^3	1031
UA	HEX overall conductance (LMTD)	W/K	—
$\tau_{\rm fan}$	Fan time constant	s	0.5
$W_{\rm fan,max}$	Fan speed limit	rad/s	400
$C_{\rm fan}$	Fan flow constant	-	0.001
$n_{\rm fan}$	Fan flow exponent (for axial fan)	-	1.5
$\mathrm{pwm}_{\rm fan}$	Fan pulse width modulation command	-	[0,1]
$k_{\rm T}$	Pump torque constant	N m/A	4.77×10^{-2}
$k_{\rm e}$	Pump back-EMF constant	V s/rad	4.77×10^{-2}
$R_{\rm m}$	Motor resistance	Ω	0.3
$L_{\rm m}$	Motor inductance	H	3×10^{-3}
$V_{\rm s}$	Supply voltage	V	48
J	Motor & impeller inertia	kg m^2	—
$\sigma_{\rm y}$	Meas. noise std (per channel)[1]	-	[0.1, 0.1, 0.1, 0, 0.1, 0.1]
$n_{\rm f}$	Number of faults	-	4

[1] Channels: [$T_{\rm fc}$, $T_{\rm h,out}$, $T_{\rm c,out}$, $W_{\rm pump}$, $I_{\rm pump}$, $W_{\rm fan}$].

air exiting the HEX, $T_{\rm c,out}$. Heat exchanger and actuator dynamics are captured with first-order energy balances and low-order motor models, consistent with control-oriented HEX modelling practice [13]. The PEMFC stack energy balance can be written as

$$\dot{T}_{\rm fc} = \frac{1}{m_{\rm fc} c_{\rm p,fc}} \left(Q_{\rm pemfc} - \dot{m}_{\rm h} c_{\rm p} (T_{\rm fc} - T_{\rm h,out})\right) \tag{1}$$

The Log Mean Temperature Difference (LMTD) method is used to define the overall heat transfer coefficient UA for cross flow

$$\begin{aligned} \Delta T_1 &= T_{\rm h,in} - T_{\rm c,out}, \\ \Delta T_2 &= T_{\rm h,out} - T_{\rm c,in}, \end{aligned} \tag{2}$$

$$\Delta T_{\rm LMTD} = \frac{\Delta T_1 - \Delta T_2}{\ln\left(\frac{\Delta T_1}{\Delta T_2}\right)} \tag{3}$$

and the coolant energy balance is given by

$$\begin{aligned} \dot{T}_{\rm h,out} = \frac{1}{m_{\rm h,HEX} c_{\rm p,coolant}} &(\dot{m}_{\rm h} c_{\rm p,coolant} (T_{\rm h,in} - T_{\rm h,out}) \\ &- UA\, \Delta T_{\rm LMTD}). \end{aligned} \tag{4}$$

$T_{\rm h,in}$ is the temperature of the coolant after the conditioning of the inlet fuel and air to PEMFC. The heat removed by conditioning is

$$Q_{\rm cond} = \dot{m}_{\rm h} c_{\rm p,coolant} (T_{\rm fc} - T_{\rm h,in}). \tag{5}$$

The cold-side (air) energy balance is given by

$$\begin{aligned} \dot{T}_{\rm c,out} = \frac{1}{m_{\rm air} c_{\rm p,air}} &(\dot{m}_{\rm air} c_{\rm p,air} (T_{\rm c,in} - T_{\rm c,out}) \\ &+ UA\, \Delta T_{\rm LMTD}). \end{aligned} \tag{6}$$

2.2. Actuator modelling

The coolant mass flow and air mass flow are driven by the actuators. Here, pump and fan mass flows are defined in terms of the pump speed and fan speed, respectively:

$$\begin{aligned} \dot{m}_{\rm h} &= \rho_{\rm coolant} k_Q w_{\rm pump}, \\ \dot{m}_{\rm air} &= C_{\rm fan}\, w_{\rm fan}^{n_{\rm fan}}. \end{aligned} \tag{7}$$

Pump dynamics are defined by pump speed and pump current [14]

$$\dot{w}_{\rm pump}(t) = \frac{1}{J} \left(k_{\rm T}\, I_{\rm pump}(t) - k_{\rm L}\, w_{\rm pump}^2(t)\right), \tag{8}$$

$$\dot{I}_{\rm pump}(t) = -\frac{1}{L_{\rm m}} \left(R_{\rm m}\, I_{\rm pump}(t) + k_{\rm e}\, w_{\rm pump}(t) - V_a\right), \tag{9}$$

where V_a is the applied voltage and can also be written in terms of pulse width modulation (PWM) command. The fan is modeled as a first-order speed actuator

$$\dot{w}_{\rm fan} = -\frac{1}{\tau_{\rm fan}} w_{\rm fan} + \frac{W_{\rm fan,max}}{\tau_{\rm fan}} \mathrm{pwm}_{\rm fan}. \tag{10}$$

2.3. State-space model and linearisation

The first order equations of TMS are then used to create a nonlinear state space model with states given as

$$x = \begin{bmatrix} T_{\rm fc} & T_{\rm h,out} & T_{\rm c,out} & w_{\rm pump} & I_{\rm pump} & w_{\rm fan} \end{bmatrix}^\top. \tag{11}$$

The model inputs are the PWM commands for pump speed and fan speed

$$u = \begin{bmatrix} u_1 & u_2 \end{bmatrix}^\top, \tag{12}$$

and the disturbances are the heat rejected to the PEMFC stack and the heat used for conditioning of the PEMFC inlets,

$$d = \begin{bmatrix} Q_{\text{pemfc}} & Q_{\text{cond}} \end{bmatrix}^\top . \tag{13}$$

Lastly four faults are modeled as explained in Table 2 are coolant line clogging, pump degradation, fan degradation, and coolant leakage

$$f = \begin{bmatrix} \alpha_{\text{clog}} & \delta_{\text{pump}} & \delta_{\text{fan}} & \ell_{\text{leak}} \end{bmatrix}^\top . \tag{14}$$

The nonlinear discrete model is $x_{k+1} = g(x_k, u_k, d_k, f_k)$ with outputs $y_k = Cx_k$. It is then linearised around the operating point $(x_0, u_0, d_0, 0)$ which gives

$$\Delta x_{k+1} = A\,\Delta x_k + B\,\Delta u_k + E_d\,\Delta d_k + E_f\,\Delta f_k, \tag{15}$$

with $y_k = Cx_k$ and $C = I_6$ for the measured states in this work. Matrices (A, B, E_d, E_f) are obtained from the Jacobians of $g(\cdot)$ and evaluated at the operating point.

2.4. Unknown input observer design

For each fault f_j, $j \in \{1, \ldots, n_f\}$, an UIO is built that rejects all exogenous disturbances and the other faults. Let

$$E_{\text{rem}} = [E_d \;\; E_f(:, \mathcal{I} \backslash \{j\})] \tag{16}$$

A sufficient decoupling condition is

$$\operatorname{rank}\big(C\,E_{\text{rem}}\big) = \operatorname{rank}\big(E_{\text{rem}}\big). \tag{17}$$

Pick

$$\begin{aligned} H_j &= E_{\text{rem}}(CE_{\text{rem}})^\dagger , \\ T_j &= I - H_j C, \end{aligned} \tag{18}$$

where $(\cdot)^\dagger$ is a regularised pseudoinverse.
With $A_{1j} = T_j A$, choose K_{1j} such that $F_j = A_{1j} - K_{1j}C$ is stable. Define $K_j = K_{1j} + F_j H_j$.
The observer and state estimate are

$$z_{j,k+1} = F_j z_{j,k} + T_j B\,\Delta u_k + K_j(y_k - Cx_0), \tag{19}$$

$$\begin{aligned} \widehat{\Delta x}_{j,k+1} &= z_{j,k+1} + H_j(y_k - Cx_0), \\ \hat{x}_{j,k} &= x_0 + \widehat{\Delta x}_{j,k}. \end{aligned} \tag{20}$$

A structured residual uses a row W_j in the left-nullspace of CE_{rem}:

$$\begin{aligned} r_{j,k} &= W_j[y_k - C\hat{x}_{j,k}] , \\ W_j(CE_{\text{rem}}) &= 0. \end{aligned} \tag{21}$$

W_j is selected to maximize sensitivity to the target fault, e.g. pick the row of a basis of $\mathcal{N}((CE_{\text{rem}})^\top)^\top$ that maximizes $\|W_j\,C\,E_f(:, j)\|_2$.

2.5. Residual conditioning and detection logic

The bank of UIOs provide a state estimate $\hat{x}_{j,k}$ at discrete time k with sampling period t_s as shown in equation 21. Fault detection is performed on a causal, trailing moving average of the residual magnitude to suppress high-frequency noise while preserving step-like changes:

$$\begin{aligned} m_{j,k} &\triangleq \frac{1}{M_k} \sum_{i=0}^{M_k-1} \big\|r_{j,k\text{-}i}\big\|_1, \\ M_k &= \min\{M,\, k{+}1\}, \end{aligned} \tag{22}$$

where $M \in \mathbb{N}$ is the window length and $\|\cdot\|_1$ is the entry-wise ℓ_1 norm. The definition in equation (22) is causal and well-defined from the first sample.
The adaptive threshold per-UIO is derived from pre-fault/non-faulty residual data. Let $\mathcal{B} = \{1, \ldots, k_{\text{inj}}{-}1\}$ denote the pre-injection baseline interval, with k_{inj} being the (known) fault-injection index. For each observer, compute the baseline median and the median absolute deviation (MAD):

$$\begin{aligned} \text{med}_j &\triangleq \text{median}\{\, m_{j,k} : k \in \mathcal{B}\,\}, \\ \text{MAD}_j &\triangleq \text{median}\big\{|m_{j,k} - \text{med}_j| : k \in \mathcal{B}\big\} + \varepsilon \end{aligned} \tag{23}$$

with a small $\varepsilon > 0$ to avoid degenerate thresholds. The decision threshold is

$$\text{TH}_j \triangleq \max\Big(\,\text{med}_j + \kappa\, c_{\text{MAD}}\, \text{MAD}_j,\;\, \text{TH}_{\min}\Big), \tag{24}$$

where $\kappa > 0$ sets the sensitivity and c_{MAD} is the Gaussian consistency factor that maps MAD to a standard-deviation scale.
To mitigate spurious crossings due to noise, a persistence rule is defined. This means, a detection is declared only after L consecutive samples above the threshold. Define

$$\begin{aligned} a_{j,k} &\triangleq \{m_{j,k} > \text{TH}_j\} , \\ s_{j,k} &\triangleq \sum_{i=0}^{L-1} a_{j,k\text{-}i}, \end{aligned} \tag{25}$$

and record the first index

$$\begin{aligned} k_{\text{det},j} &= \min\big\{k \geq k_{\text{inj}} : s_{j,k} \geq L\big\}, \\ t_{\text{det},j} &= \big(k_{\text{det},j} - k_{\text{inj}}\big)\, t_s. \end{aligned} \tag{26}$$

If the set is empty, no detection is reported for observer j.

3. RESULTS AND DISCUSSION

This section validates the linearised PEMFC thermal-management model desiged in section 2.3 and demonstrates robust fault detection/isolation using a bank of UIOs. Unless stated otherwise, the simulation uses a sampling time $t_s = 0.002$ s and N=10,000 samples (20 s). Faults are injected at k_{inj}=2000 (4 s), and a heat-input step $\Delta d_1 = 50$ kW is applied at $t_{dist} = 4$ s on the stack thermal balance.
Figure 3 compares the response of the nonlinear plant with its linearised counterpart for the heat-input step. All six states $\{T_{\text{fc}}, T_{\text{h,out}}, T_{\text{c,out}}, W_{\text{pump}}, I_{\text{pump}}, W_{\text{fan}}\}$ are shown (nonlinear: solid; linearised: dashed). The two models exhibit nearly identical dynamics around the operating point.
For each state x_i, the root mean square error (RMSE) and normalized RMSE (NRMSE) are computed as

$$\text{RMSE}(x_i) = \sqrt{\tfrac{1}{M} \sum_{k=k_0}^{k_1} \big(x_{i,k} - \hat{x}_{i,k}\big)^2} \tag{27}$$

$$\text{NRMSE}(x_i) = \frac{\text{RMSE}(x_i)}{\max_k x_{i,k} - \min_k x_{i,k}} \tag{28}$$

TAB 2. Actuator faults: meaning, injection in the model, and test values.

Fault	Physical meaning	Injected in state update	Value	UIO
α_{clog}	Pump clog: added hydraulic drag (higher quadratic loss)	$k_{\mathrm{L}} \mapsto k_{\mathrm{L}}(1+\alpha_{\mathrm{clog}})$ in Eq 8	0.4	UIO1
δ_{pump}	Loss of pump actuation / pump degradation: effective motor voltage reduced	$u_1 \mapsto (1-\delta_{\mathrm{pump}})\, u_1$ in Eq 9	0.2	UIO2
δ_{fan}	Loss of fan actuation: PWM–speed effectiveness reduced.	$V_a \mapsto (1-\delta_{\mathrm{fan}})\, V_a$ in Eq 10	0.2	UIO3
λ_{leak}	Coolant bypass/leak: effective hot–side flow through HEX reduced	$\dot{m}_{\mathrm{h}} \mapsto (1-\ell_{\mathrm{leak}})\dot{m}_{\mathrm{h}}$ in Eq 4	0.5	UIO4

All faults are dimensionless in range $[0, 1)$ unless noted, where $0 =$ healthy.

TAB 3. Symbols and user-selected parameters (with typical settings)

Symbol setting	Meaning	Typical
W_{j}	Projection matrix for UIO j	–
$r_{\mathrm{j,k}}$	Projected residual (21)	–
$m_{\mathrm{j,k}}$	Causal smoothed magnitude (22)	–
$\mathrm{TH_j}$	Adaptive threshold (24)	–
L	Persistence run length (samples)	10–50
k_{inj}	Fault-injection index	$2000(\approx 4\ s)$
$k_{\mathrm{det},j}$, $t_{\mathrm{det},j}$	Detection index/time (26)	–
M	Moving-average window (samples)	$\lfloor [0.4, 2]\,\mathrm{s}/t_{\mathrm{s}} \rfloor$
κ	MAD scaling factor in threshold	4–8
$\mathrm{TH_{min}}$	Hard floor on the threshold	sensor quantisation

Guidance: Larger $M \Rightarrow$ smoother, slower response; larger κ reduces false alarms; $\mathrm{TH_{min}}$ avoids vanishing thresholds; choose L using the dominant time constant and M.

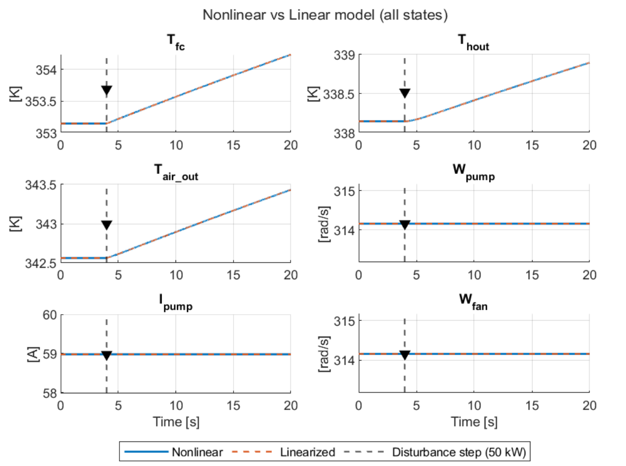

FIG 3. Nonlinear vs linearised system response under disturbance step change

over $t \in [0, 20]$ s with normalization by the pre-fault steady value $x_i^{\star}$.
All states satisfy NRMSE $< 5\%$, confirming that the linearised model is an accurate local approximation and suitable for observer and FDD design.
Figure 5 shows m_{j} for all UIOs under the disturbance step Δd_1 with no injected faults. All trajectories remain below their thresholds throughout, including after t_{dist}, demonstrating immunity to normal operating disturbances and absence of false alarms. Figure 4 illustrates the temperature tracking performance of the UIO bank in the presence of sensor noise and a Δd_1 heat disturbance applied at t_{dist}. Measurements are corrupted with zero-mean white noise (per-channel standard deviations σ_y in the units of each sensor) and plotted as a shaded $\pm 3\sigma$ band. It can be seen that the observers remain tightly aligned with the true out-

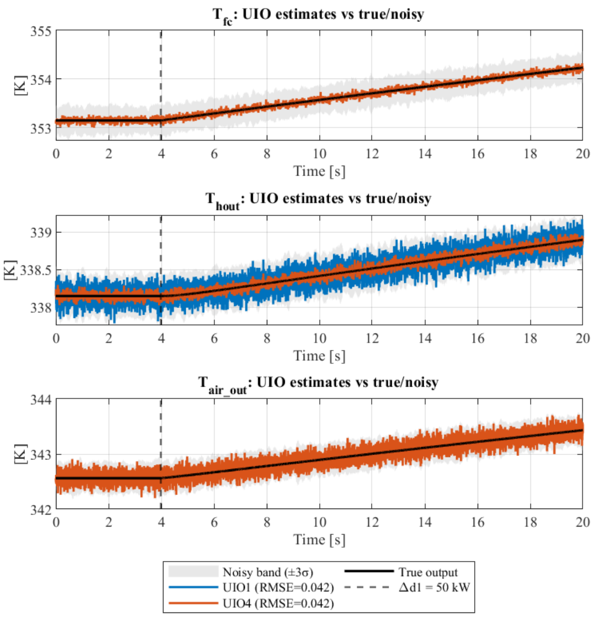

FIG 4. Observer output vs Noisy Measurement – Temperatures

puts across all temperature channels and lie well within the noisy measurement envelope, with RMSE values on the order of 0.04–0.10 K. These results clearly demonstrate that all UIOs are capable of accurately reproducing the system dynamics despite noise and disturbances, thereby validating their suitability for robust residual generation and subsequent fault detection.
To evaluate the effect of the structured projection, we compared residual–based detection using the left–nullspace weighting matrix W (projected residual) against an unstructured baseline that relies directly on the innovation norm. Thresholds in both cases were computed from the pre–fault baseline/non-faulty data using robust MAD statistics, with persistence enforced over a fixed window. As shown in figure 6 the comparison highlights two important trends: (i) for Fault 1 with UIO1, the unstructured residual fails to cross the threshold, resulting in a missed detection, whereas the W–projected residual produces a clear threshold crossing; and (ii) for Fault 4 with UIO4, both methods succeed, but the projected residual detects significantly earlier, with a larger margin above threshold. These examples illustrate the general finding that the W–projection enhances sensitivity to the intended fault.
Figure 7 plots m_{j}(solid) and TH_j(dashed) for all fault vs. UIO combinations. Immediately after fault injection at k_{inj} the residual corresponding to the sensitive UIO rises above threshold while others remain below; markers annotate absolute detection time and delay relative to fault onset. The UIO bank consistently detects the intended

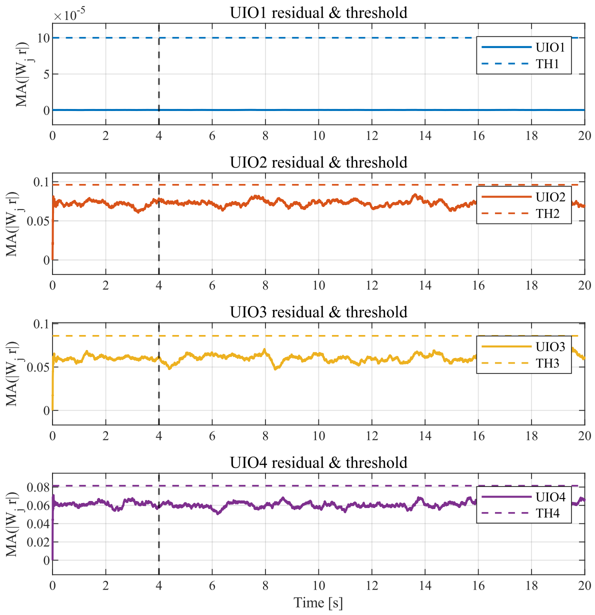

FIG 5. UIO thresholds and residuals under disturbance step change

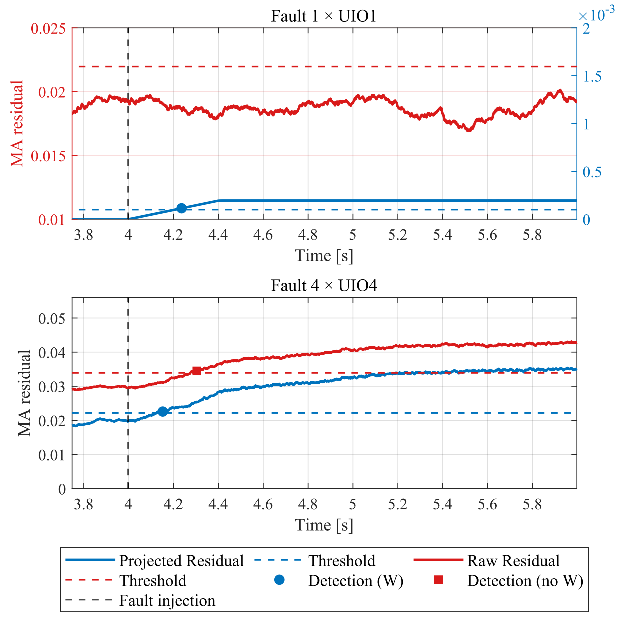

FIG 6. Comparison between projected residual and raw residual based fault detection

fault while avoiding off-diagonal alarms, thereby achieving reliable isolation. A quantitative summary (detection rates, delays, and false alarm rate) is reported in Table 4.

4. CONCLUSION AND OUTLOOK

This work has demonstrated the feasibility of a model-based fault detection and diagnosis framework for TMS-enabling components within an EAP system. The observer bank was systematically evaluated through Monte-Carlo fault injection, providing quantitative insight into detection rates, delay distributions, and robustness margins. The results confirm that each intended UIO consistently detects its target fault with high reliability, while cross-detection by non-intended observers is effectively suppressed. Detection delays were shown to be negligible compared to the dominant system dynamics. The residual-to-threshold ratios highlight clear separation between healthy and faulty conditions. Primarily, the framework exhibited zero false alarms over repeated noise realizations, underlining the robustness of the threshold design. At the same time, some limitations were observed.

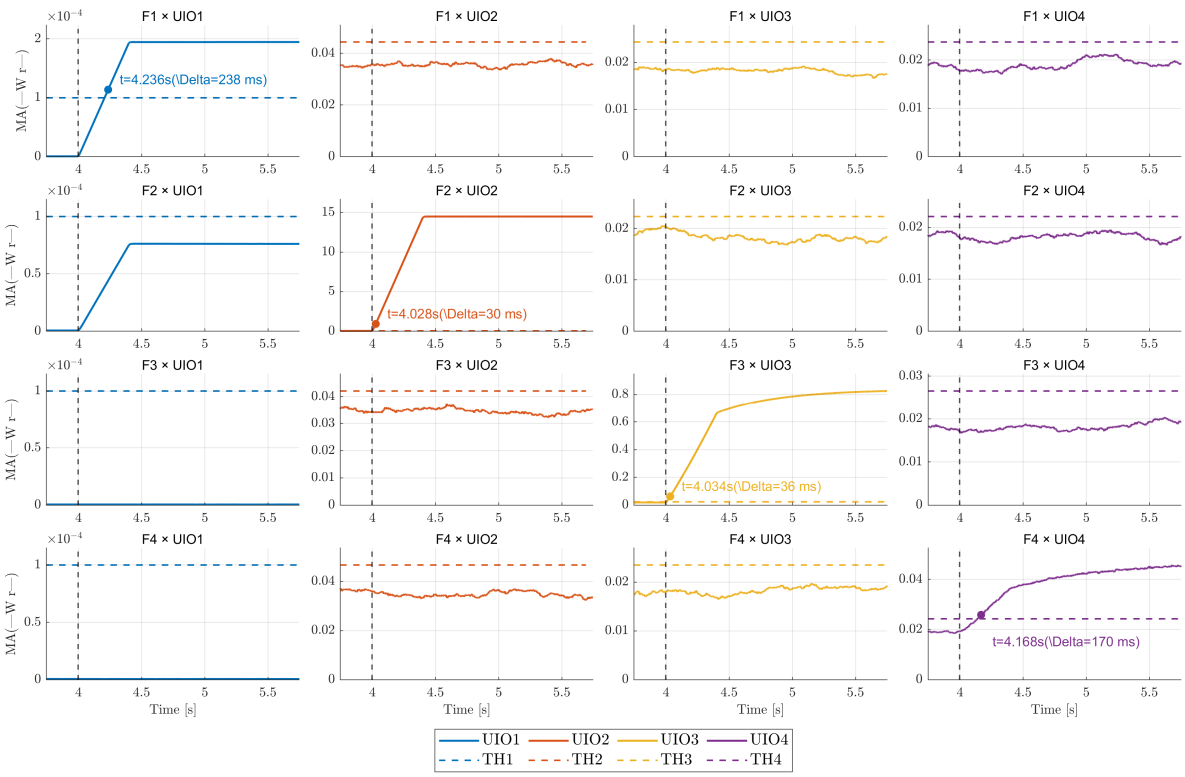

FIG 7. UIO bank residual under presence of each fault and threshold crossing

TAB 4. Detection performance of the UIO bank over $R = 20$ Monte–Carlo runs.

Fault	UIO	Detected [%]	Delay mean [s]	Max/θ	False alarms
F1	UIO1	100.0	0.24 ± 0.00	1.95×	0
F1	others	0.0	—	—	0
F2	UIO2	100.0	0.03 ± 0.00	152.55×	0
F2	others	0.0	—	—	0
F3	UIO3	100.0	0.05 ± 0.00	10.54×	0
F3	others	0.0	—	—	0
F4	UIO4	100.0	2.62 ± 2.86	1.11×	0
F4	others	0.0	—	—	0

"Detected" is the percentage of runs in which the fault was detected by the given UIO. "Delay mean" is the mean ± standard deviation of the detection delay relative to the fault injection time. "Max/θ" is the peak moving–average residual relative to its robust threshold. "False alarms" is the count of false triggers observed in R no–fault runs.

Faults were introduced one at a time with fixed magnitudes, which simplifies the diagnostic setting compared to real operation. In particular, for Fault 4 the detection probability dropped significantly when the measurement had Gaussian noise for injected fault value below 50%, suggesting a sensitivity limit in the residual dynamics. These constraints highlight the need for further development to handle simultaneous or time–varying faults and to systematically characterize detection thresholds versus fault magnitudes. Future work will address these aspects by exploring multi–fault scenarios, scalable threshold adaptation strategies, and experimental validation on real TMS hardware. In addition, the integration of the FDD module with fault–tolerant control will be pursued, enabling the controller to adjust outputs in real time based on diagnostic feedback. Extensions to cover thermal faults associated with heat sources in the EAP will also be undertaken, as such faults are expected to introduce more complex coupled dynamics.

Contact

zalakben.barot@dlr.de

References

[1] Farab Quaium, Thomas Bielsky, and Frank Thielecke. Fuel cell cooling system design for hydrogen-powered concept aircraft. In Deutscher Luft- und Raumfahrtkongress (DLRK) 2022, Dresden, Germany, 2024. Deutsche Gesellschaft für Luft- und Raumfahrt - Lilienthal-Oberth e.V. (DGLR). Published by DGLR in 2024; event held in 2022. URN: urn:nbn:de:101:1-2412161452049.584635110258. DOI: 10.25967/570127.

[2] Steven G Goebel. Evaporative cooled fuel cell, Nov. 1 2005. US Patent 6,960,404.

[3] Satish G. Kandlikar and Zijie Lu. Thermal management issues in a pemfc stack – a brief review of current status. Applied Thermal Engineering, 29(7):1276–1280, 2009. ISSN: 1359-4311. Selected Papers from the 10th UK National Heat Transfer Conference, Edinburgh, Scotland, September 10-11, 2007. DOI: https://doi.org/10.1016/j.applthermaleng.2008.05.009.

[4] Anam Abid, Muhammad Tahir Khan, and Javaid Iqbal. A review on fault detection and diagnosis techniques: basics and beyond. Artificial Intelligence Review, 54(5):3639–3664, 2021. ISSN: 1573-7462. DOI: 10.1007/s10462-020-09934-2.

[5] Rolf Isermann. Model-based fault-detection and diagnosis – status and applications. Annual Reviews in Control, 29(1):71–85, 2005. ISSN: 1367-5788. DOI: https://doi.org/10.1016/j.arcontrol.2004.12.002.

[6] S. R. Hashemi, R. Esmaeeli, A. Nazari, H. Aliniagerdroudbari, M. Alhadri, W. Zakri, A. H. Mohammed, A. Mahajan, and S. Farhad. A fast diagnosis methodology for typical faults of a lithium-ion battery in electric and hybrid electric aircraft. Journal of Electrochemical Energy Conversion and Storage, 17(1):011011, 10 2019. ISSN: 2381-6872. DOI: 10.1115/1.4044956.

[7] L. D. Milfont, G. Torllone de Carvalho Ferreira, and M. Giesbrecht. Fault diagnosis in electric machines and propellers for electrical propulsion aircraft: A review. Engineering Applications of Artificial Intelligence, 139:109577, 2025. ISSN: 0952-1976. DOI: https://doi.org/10.1016/j.engappai.2024.109577.

[8] D. Henry, J. Cieslak, A. Zolghadri, and D. Efimov. Fault detection and diagnosis in electrical aircraft flight control system. page NC, 08 2011. DOI: 10.2514/6.2011-6679.

[9] Chizhou Yan, Jian Chen, Hao Liu, and Huaxin Lu. Model-based fault tolerant control for the thermal management of pemfc systems. IEEE Transactions on Industrial Electronics, 67(4):2875–2884, 2020. DOI: 10.1109/TIE.2019.2912772.

[10] Jin Young Park, In Seop Lim, Yeong Ho Lee, Won-Yong Lee, Hwanyeong Oh, and Min Soo Kim. Severity-based fault diagnostic method for polymer electrolyte membrane fuel cell systems. Applied Energy, 332:120486, 2023. ISSN: 0306-2619. DOI: https://doi.org/10.1016/j.apenergy.2022.120486.

[11] A. S. J. van Heerden, D. M. Judt, S. Jafari, C. P. Lawson, T. Nikolaidis, and D. Bosak. Aircraft thermal management: Practices, technology, system architectures, future challenges, and opportunities. Progress in Aerospace Sciences, 128:100767, 2022. ISSN: 0376-0421. DOI: https://doi.org/10.1016/j.paerosci.2021.100767.

[12] Stefanie De Graaf, Antje Link, and Martin Staggat. Characterisation of thermal management system specific heat rejection for electric propulsion architectures. 07 2023. DOI: 10.13009/EUCASS2023-262.

[13] Bingen Yang and Inna Abramova. Dynamic Systems: Modeling, Simulation, and Analysis. Cambridge University Press, 2022.

[14] Gordana Janevska. Mathematical modeling of pump system. 09 2013.